The EO-1
Advanced Land Imager (ALI)
Scattered Light Study Report

October 12, 1998

Prepared by:
Xindong Wang[1], Gerald Godden[2], and Shi-Yue Qiu[1]

1. Computational Physics Applications, Inc.
2. Physics Applications, Inc.

Abstract:

The EO-1 Advanced Land Imager (ALI) is the first earth-orbiting instrument to be flown NASA's new millennium program. It is a technology verification project designed to demonstrate comparable or improved Landsat spatial and spectral resolution with substantial mass, volume and cost savings. ALI is a 4 mirror, all-reflective, pushbroom type sensor configured to cover a 15 degree wide Field-of-View, when the focal plane is fully populated. This study investigated the expected scattered light performance based measurements of the BRDFs performed by Schmidt Measurement Systems for each of the four Silicon Carbide substrate, SiOx protected silver coated mirrors. The BRDF interpretations and computed Total Integrated Scatter (TIS) levels for each mirror compared closely with previous results reported by the Lambda Research Corporation under contract to the Lincoln Laboratory. The ALI Silicon Carbide M1, M2, M3 and FM BRDFs were each found to be significantly higher than the near state-of-the-art MODIS beryllium scan mirror. A detailed system-level Point Spread Function (PSF) model was developed for the Panchromatic Band, covering the 480 to 690 nanometers spectral region, and Band 3, covering the 633 to 690 micrometers spectral region. The PSF model was based on the ALI Code V sequence file configuration parameters and incorporated the BRDFs for each mirror fitted to a modified Harvey-Shack function, the ALI fore-baffle, the M2 field stop and other internal vignetting features, and configuration details of the partially populated FPA. The system level PSFs were then convolved with representations of the Landsat 7 specification scattered light scene. The scattered light radiance levels at the center of the specified scene were found to be 55% and 80% of the target radiance levels, for the Pan Band and Band 3, respectively. In terms of the low gain saturation radiance levels, the scatter levels were found to be 5.4% and 7.7%, for the Pan Bands and Band 3, respectively. When the PSF was applied to more physically realizable scenes, such as a semi-infinite straight cloud edge with an Lcloud/Ltyp contrast ratio of 22.3, it was found that the scatter levels will be greater than 10% of the Ltyp values for scene pixels 50 to 60 km from the cloud edge. These relatively high levels of scatter, extending over long distances from the specular point, suggest that efforts to restore images by applying FFT inversion techniques will require very detailed and accurate knowledge of the actual PSFs over a large spatial area, which will be difficult, considering the very challenging measurement requirements involved in this approach. However, if the ALI M1, M3 and FM mirrors had BRDFs equal to the BRDF for M2, the system-level scatter levels would be generally less than 2.2% of Ltyp near the cloud edge, and would taper off to less than 0.5% for pixels greater than 40 to 60 km from the cloud edge, depending on the pixel azimuth with respect to the ALI rectangular aperture. All results reported are based on the Schmidt Measurement Systems BRDF measurements, which presumably were performed under ideal low cleanliness level conditions. Allowances for higher system level cleanliness levels are necssary. Tools are in place to apply the PSFs to actual Landsat Earth scenes. The results reported suggest that there will be significant radiance bias errors in the vicinity of high contrast scene features.

Outline

1. Introduction and Instrument Description

The EO-1 Advanced Land Imager (ALI) is the first earth-orbiting instrument to be flown under NASA's New Millennium program. It is a technology verification project designed to demonstrate comparable or improved Landsat spatial and spectral resolution with substantial mass, volume and cost savings. Among the new technologies involved are the wide field of view (WFOV) optical design operating in a push-broom fashion, and the new diamond-turned and polished Silicon Carbide (SiC) mirror technology by SSG, both of which we will address in this report.

Operating at an orbit altitude of 705 km, the ALI is intended to cover ~185 km contiguous swath of the earth surface with a fully populated focal plane array (FPA), consistent with the 15^{o} wide FOV optical system. A schematic illustration of the ALI optical train is shown in Figure 1.1. It contains four optical mirrors: M1, M2 (defining the field stop), M3 and F1 mirror (a flat fold mirror) before the focal plane array (FPA). The push-broom data collection mode and the WFOV are designed to achieve an overall configuration with no moving parts in the entire optical train of the telescope. Each sensor chip assembly (SCA) on the FPA contains 9 multi-spectral bands and a single panchromatic band. The wavelength regions for each of these bands are shown in Table 1.1. The partially populated FPA of the ALI is shown in Figure 1.2.

The ALI optical system is configured to have an unvignetted FOV of $15^{o} \times 1.256^{o}$, as determined by the field-stop, M2. The fore-baffle in front of M1 is slightly oversized relative to the full Focal Plane Assembly (FPA) FOV. The panchromatic band detectors provide a 30 m ground instantaneous FOV (GIFOV) at nadir, and the multi-spectral band detectors provide a 10 m GIFOV at nadir.

The ALI image quality for each of the spectral bands results from the combined effects of:

- Optical image aberrations
- Instrument pointing jitter
- Scan rates and integration time smear
- Detector geometry
- Stray light from spurious reflections off out-of-field surfaces
- Mirror scattered light as characterized by each mirror's BRDF and the overall optical configuration
- Aperture diffraction
- Electronic cross-talk
- Other spurious optical effects, such as ghosting, optical crosstalk/leaks, etc.

This study concentrates on the effects on mirror scatter. To do this we determine the end-to-end Point Spread Function (PSF) due to optical scatter and the vignetting effects of the fore-baffle and optical element apertures, and then apply the PSFs to selected scenes (per specification, or from Landsat images), to determine radiance errors in the convolved scene relative to the input scene We do not address other potentially important effects. We use the Code V optical system description (sequence files) provided by Lincoln Laboratory, and the mirror BRDFs measured by Schmidt Measurement Systems (SMS).

The Lambda Research Corporation (LRC), under contract to MIT Lincoln Laboratory, has carried out a similar analysis. The present report is intended to provide an independent study with further emphasis on interpretation of the results, and application of the derived PSFs to selected scenes, to assist evaluating the implication of scatter to remote sensing research products. We have developed an efficient numerical algorithm, to accurately determine the PSF for two of the ALI spectral bands (the Panchromatic band, and Band 3).

In the following sections of this report we first discuss the BRDF data by Schmidt Measurement Systems and the analytic functions used to fit these data We compare ALI diamond-turned and polished SiC mirror technology scatter performance to the current MODIS conventional polish nickel-plated Beryllium technology in terms of a Total Integrated Scatter (TIS) parameter. We then describe our approach and formalism for computing the PSF for each mirror, and the end-to-end PSF. The PSF for each mirror is presented graphically, together with the end-to-end system level PSF which includes vignetting for each mirror.

We use the system-level PSF to investigate compliance the ALI compliance with various specifications, particularly with respect to that outlined in the Landsat 7 system specification, Revision K. We further investigate ALI performance near high contrast cloud edge scenes. We then present a brief analysis for a more realistic scene. Finally, we summarize our results, conclusions and recommendations in the Summary section.

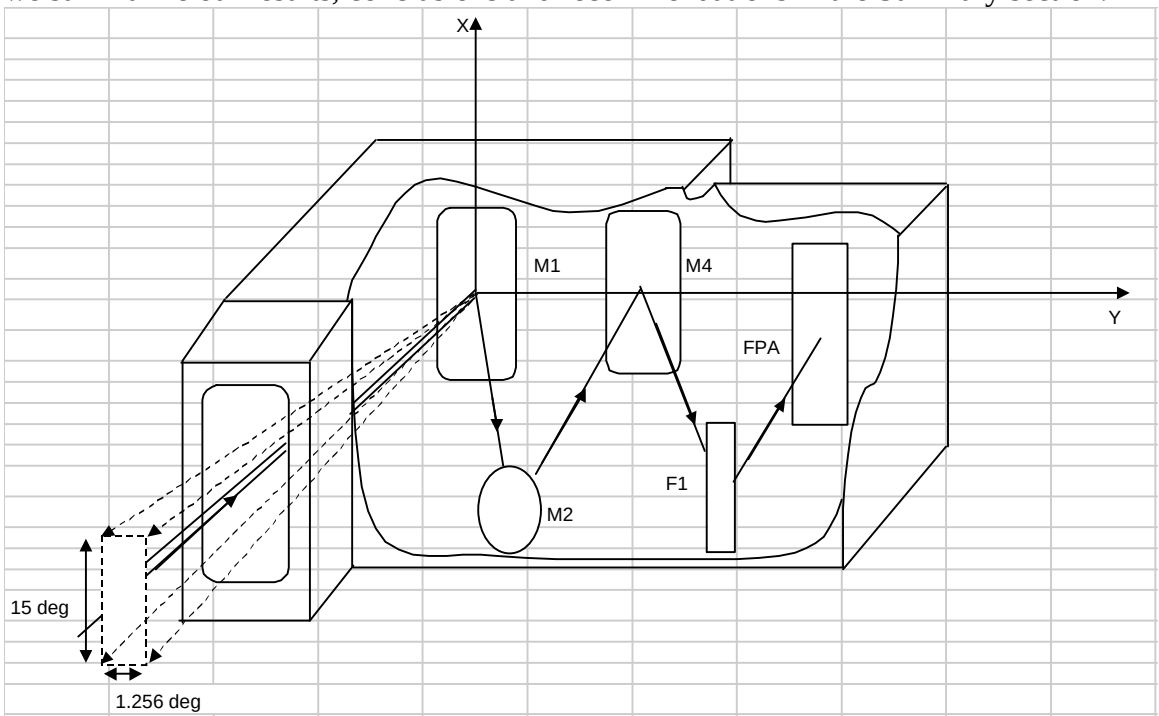

Figure 1.1 Schematic illustration of the ALI telescope.

.

Table 1.1 Spectral definition of the ALI bands

band	pan	1’	1	2	3	4	4’	5’	5	7
λ (μm)	0.48-0.69	0.433-0.453	0.45-0.515	0.525-0.605	0.633-0.69	0.775-0.805	0.845-0.89	1.2-1.3	1.55-1.75	2.08-2.35

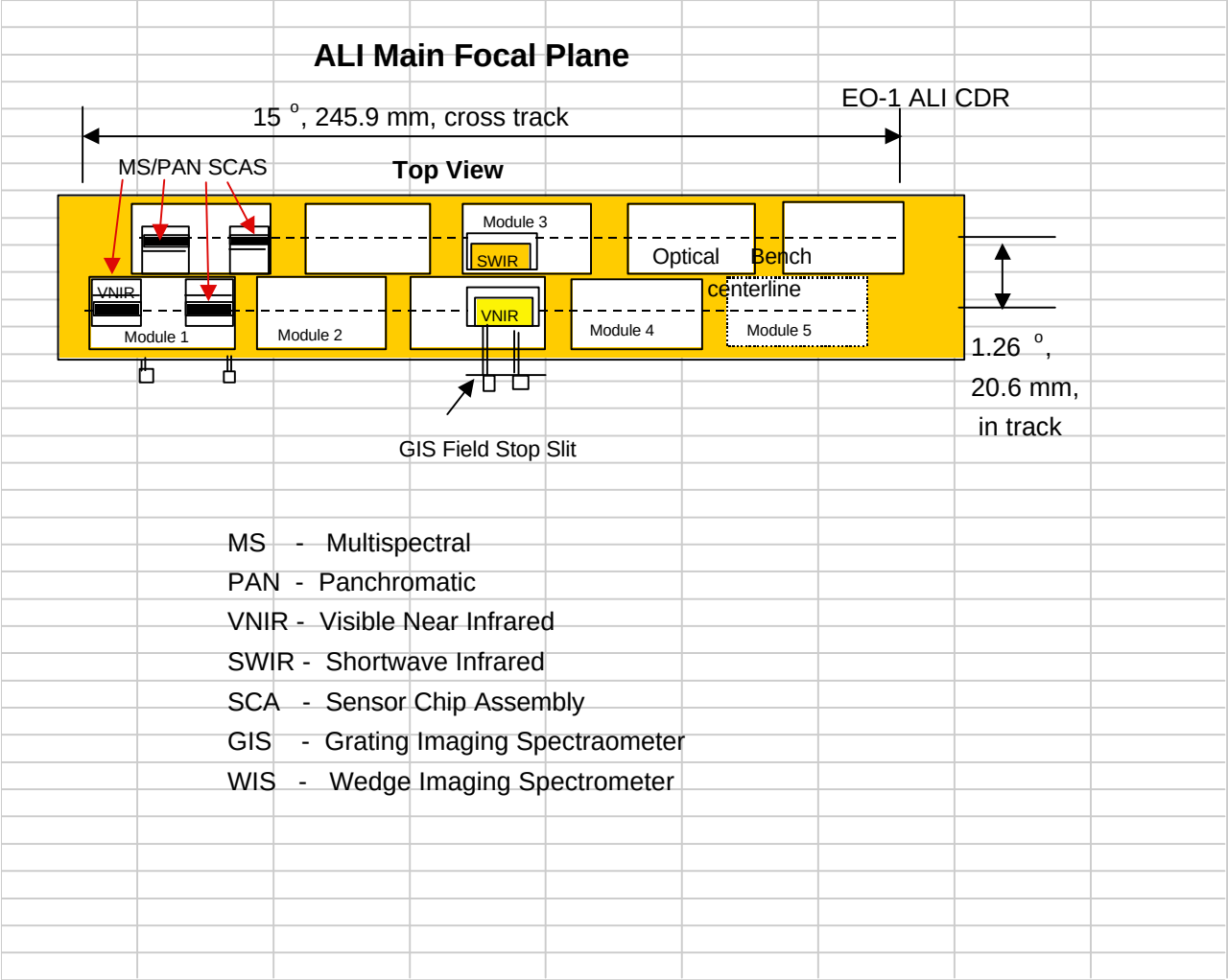

Figure 1.2 Partially populated FPA of the ALI

2. Analytic Representation and Interpretation of the Measured BRDF Data

The measured BRDF data for mirrors M1, M2, M3 and F1 are provided by Schmidt Measurement Systems. These data were fitted using the generalized Harvey-Shack (HS) model, also referred to as the ABg model:

$$(2.1) \qquad BRDF(|\vec{b}-\vec{b}_0|)=\frac{A}{B+|\vec{b}-\vec{b}_0|^g}.$$

The HS model is recovered when B=0. Here β and β_0 are the projection of the unit vectors, in the scattering direction and the specular direction respectively, onto the surface of the mirror. This model has the advantage over the HS model in that by adding one more parameter to the model, it allows a larger parameter space for fitting and thus more faithful representation of the data. It also avoids the apparent singularity in the HS model when β coincides with β_0.

The raw scatterometer data and instrument function were measured from -90^o to $+80^o$ with an incidence angle of 5°, using a 633 nm illumination source, at three spots for each mirror. Using the instrument function data, we are able to discard those small angle data points coming from the convolution of the specular beam by the instrument function. We also discarded those data points vignetted by the measuring instrument as evident by the dramatic drop of intensity near the incident angle noted by Schmidt. We then calculated $|\beta-\beta_0|$ from the given incident and scattering angles. The data points for all three spots on one mirror were then combined together into one data set.

An important measure of mirror scatter is the Total Integrated Scatter (TIS). The TIS defined by

$$(2.2) \qquad TIS=\int_0^{p/2}\sin(q)dq\int_0^{2p}dj\;\; BRDF(q,j;q_0,j_0)\cos(q),$$

where the polar angles are measured with respect to the mirror normal axis. TIS represents the total scatter into the hemispherical space surrounding the mirror normal. To obtain the best estimate possible for the TIS, requires the best-fit representation of the multiple BRDF measurements. Since the scatterometer data points were not evenly distributed, we apply a weighting function from the polar integration integrand, and minimize the following chi-square function:

$$(2.3) \qquad c^2(A,B,g)=\sum_{data}\left|\frac{A}{B+\left|\vec{b}-\vec{b}_0\right|^g}-BRDF^{measured}\right|^2\sin(q)\cos(q).$$

The resulting fitting parameters (A,B, and g) are listed in Table 2.1 together with the results obtained by LRC. Table 2.1 also gives the TIS values calculated from Equation (2.2) using the corresponding set of parameters for each mirror.

Figures 2.1-2.4 show the results of our fitting. In searching for the set of A, B, and g parameters that minimize Equation (2.3), we have confined the parameter space to within the positive numbers only. In some cases, whenever a negative B will give a smaller number for χ, a small fixed number 1×10^{-10} is used and not allowed to change in the fitting process. As shown in the Table 2.1, the TIS values calculated from our fitting

results agree fairly well with the Lambda results despite the slightly different fitting procedures used.

Table 2.1 BRDF model parameters and corresponding TIS for ALI Mirrors

	Present Work				Lambda Research Corporation Results			
	M1	M2	M3	F1	M1	M2	M3	F1
A	1.66E-03	1.00E-04	1.57E-03	5.94E-04	1.50E-03	1.00E-04	1.50E-03	5.00E-04
B	2.63E-05	1.00E-10	1.88E-03	7.33E-03	1.50E-05	1.00E-05	1.40E-03	4.00E-03
g	1.84	1.69	2.14	1.59	1.9	1.7	2.1	1.6
TIS	0.0388	0.0019	0.0365	0.0063	0.0415	0.0018	0.0351	0.0057

The Total Integrated Scatter (TIS) for a single mirror can be interpreted as a probability . The light reflected and Here, we would like to address the physical meaning of the TIS. The light received by a detector aimed at certain target pixel can be categorized into two types, the specular and the stray light. The specular light is from the target scene by specular mirror reflection (or lens refraction) only. The stray light is from the off-pixel scene due to mirror scattering, optical diffraction, etc. If we assume that the scattering is the dominant source of stray light as we did in this report, the TIS defined in Equation (2.2) is a quantitative measure of the scattering effect of a mirror. Thus the smaller the TIS for a mirror, the higher quality it has. Also note that for a mirror, the TIS is calculated only for the semi-spherical space which implies an underlying assumption of zero transmittance of the mirror. From the TIS obtained as shown in Table 2.1, we would expect the stray light contribution to be dominated by scatterings from M1 and M3 mirrors.

From the TIS values for each mirror we can see that mirrors M2 and F1 are significantly lower scatter mirrors than mirrors M1 and M3.

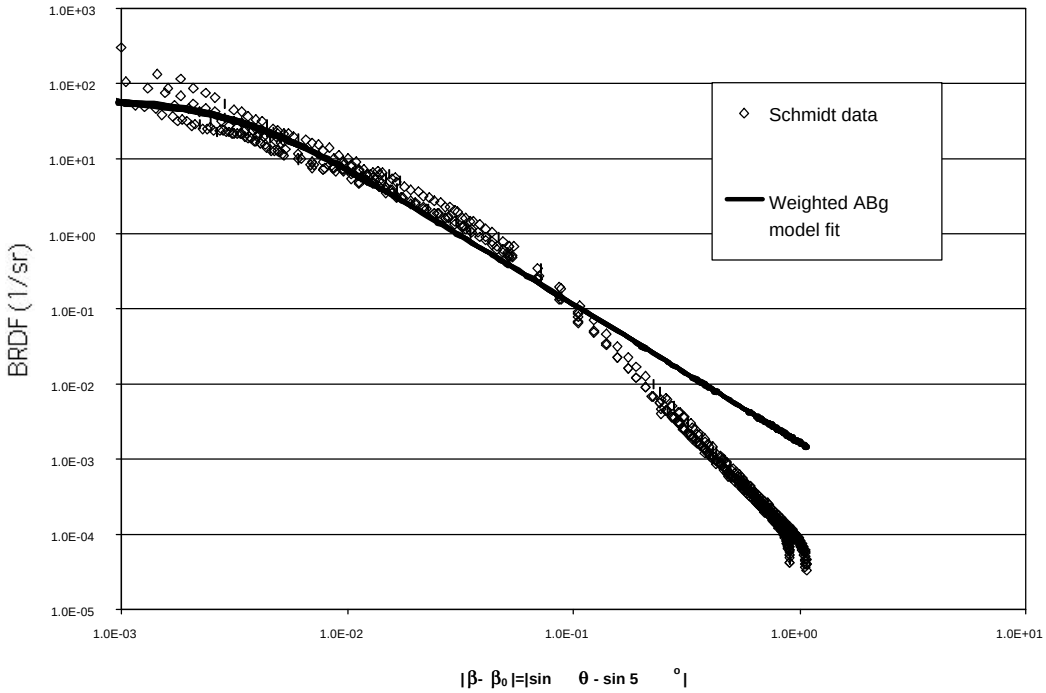

Figure 2.1: Measured BRDF for 3 spots on mirror M1 and weighted ABg model analytic fit to the data. Note the applied weighting function described in the text forces a better fit in the center region.

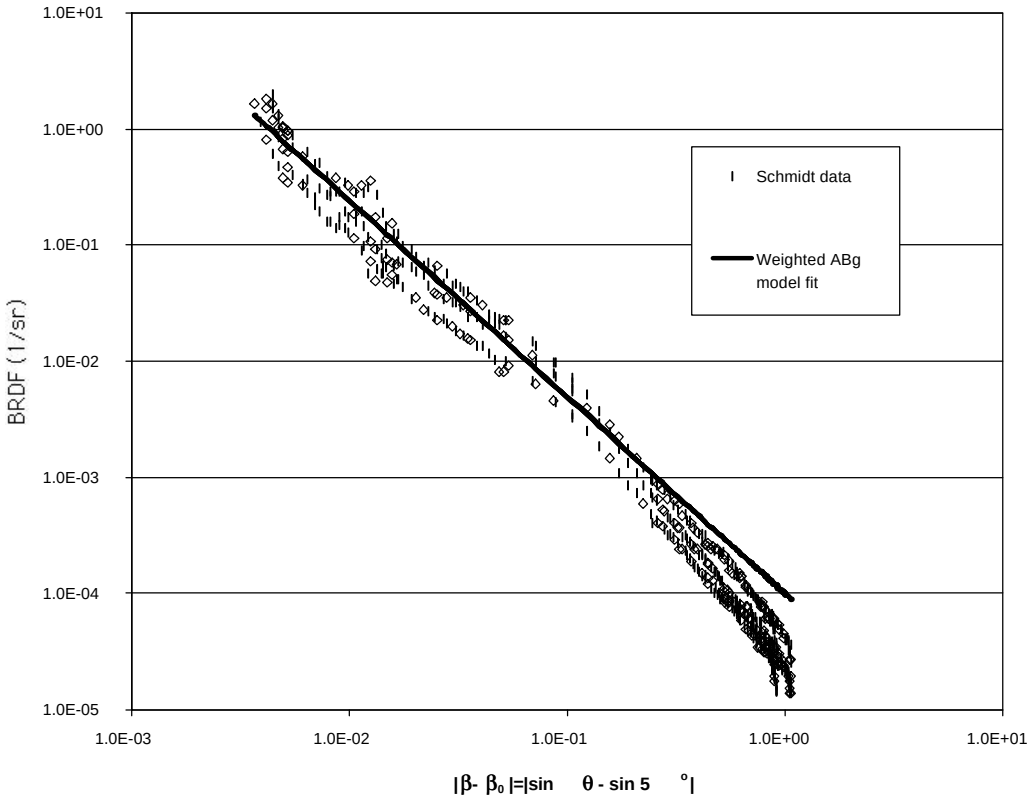

Figure 2.2: Measured BRDF for 3 spots on mirror M2 and weighted ABg model analytic fit to the data.

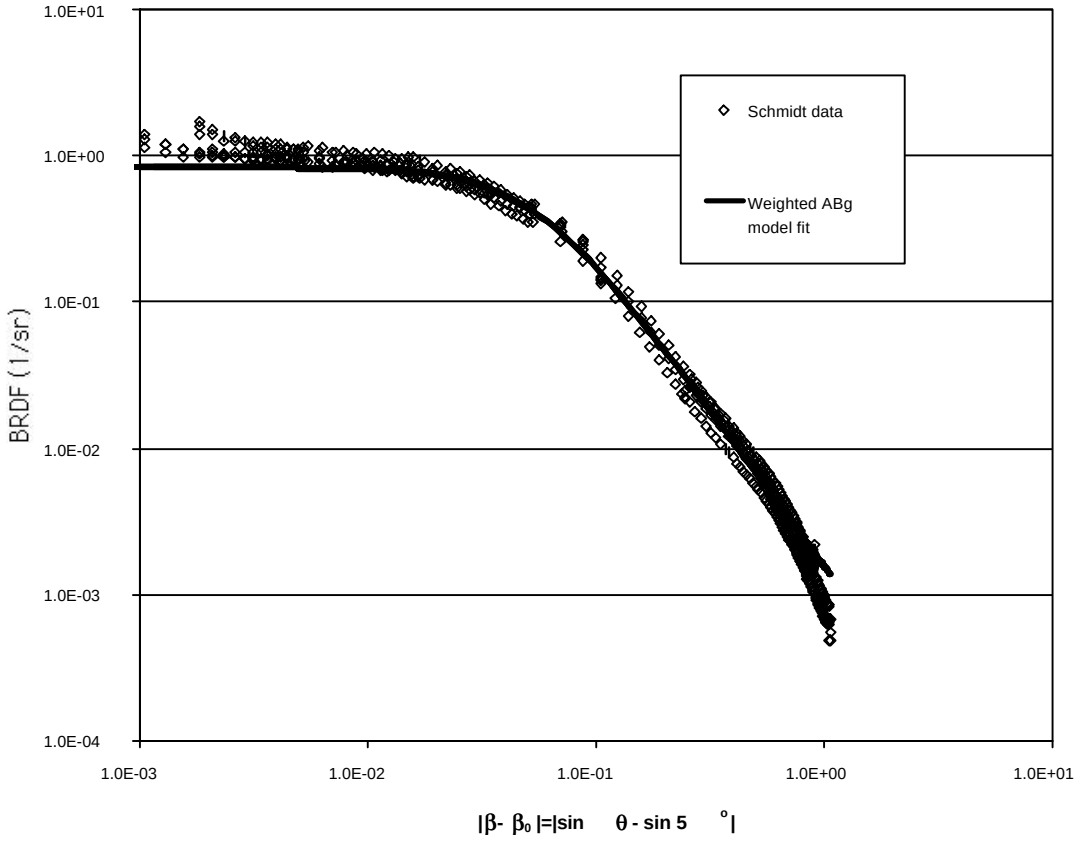

Figure 2.3: Measured BRDF for 3 spots on mirror M3 and weighted ABg model analytic fit to the data.

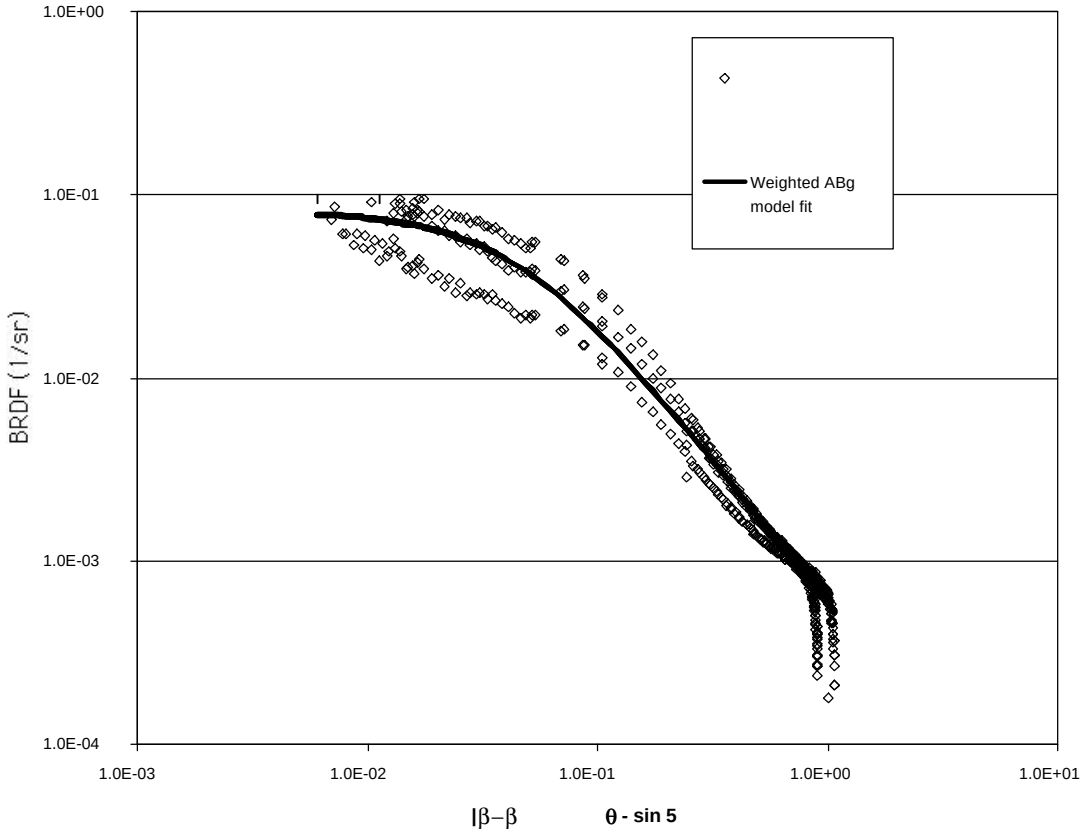

Figure 2.4: Measured BRDF for 3 spots on mirror F1 and weighted ABg model analytic fit to the data.

We would like to compare the BRDF of the SiC mirrors used in the ALI with the BRDF of the Moderate resolution Imaging Spectro-radiometer (MODIS) FM2 scan mirror which is considered state of the art Be/Ni mirrors. Figure 2.5 is a plot of BRDF versus $|\beta-\beta_0|$ for the MODIS FM2 scan mirror and the ALI M1 and M2 mirrors. Clearly the MODIS FM2 scan mirror is much better than the ALI M1 mirror and is even better than the best of the ALI mirrors, the M2 mirror. The TIS of the MODIS FM2 scan mirrors is estimated to be around 0.0005 which is substantially smaller than those of the ALI mirrors. We note, however, that this may not be an intrinsic inferiority of the SiC mirrors as is evidenced by the fact that the M2 mirror of the same material is of much higher quality than the M1 mirror. As we will see later, by substantially reducing the TIS of M1 and M3 to the level of the TIS of the M2 will dramatically improve the performance of the ALI telescope.

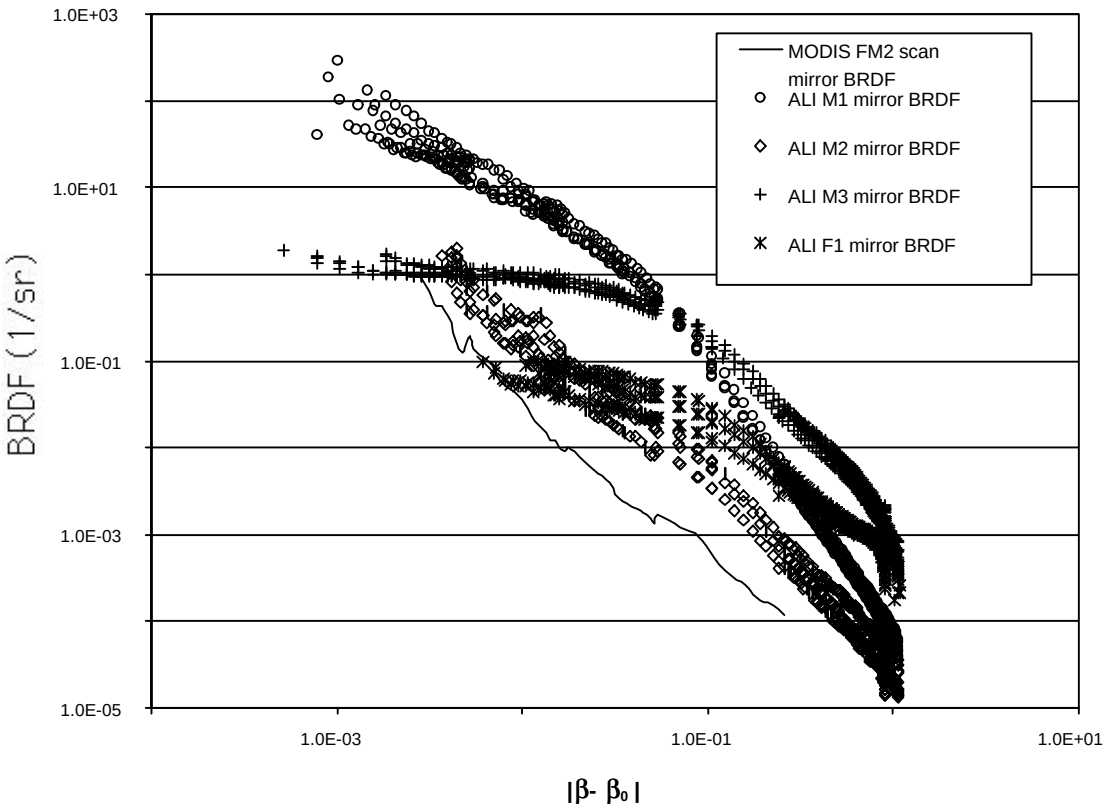

Figure 2.5 BRDF of the MODIS FM2 scan mirror and the ALI mirrors.

3. Formalism and Methodology for Determining Point Spread Functions (PSFs)

3.0 Introduction to the PSF

We define the Point Spread Function (PSF) in the following

(3.1) $$M_{\det}(\vec{t}) = \int M_{scene}(\vec{s}) \cdot PSF_{total}(\vec{s},\vec{t})\, d^2\vec{s} \quad ,$$

where $M_{scene}(\mathbf{s})$ is the actual scene radiance for the pixel at **s**, $M_{det}(\mathbf{t})$ is the detector measured radiance for the pixel at **t**. The 2-dimensional vectors in Equation 4 are related to the polar angles (θ,φ) by **s**/**t**:=(x,y)=(θ cos(φ), θ sin(φ)).

If detectors on the FPA are well-calibrated, the $PSF_{total}(\mathbf{s},\mathbf{t})$ should be normalized to one, i.e.,

(3.2) $$\int PSF_{total}(\vec{s},\vec{t})d^2\vec{s} = 1,$$

for any **t** within the designed FOV.

As we have discussed in the last section, the light received by a detector aimed at certain target pixel can be categorized into two types, the specular and the stray light. The specular light is from the target scene by specular mirror reflection (or lens refraction). The stray light is from the off-axis scene due to mirror scattering, light refraction, etc. Accordingly, we can separate the PSF into two parts, the specular light part and the stray light part

(3.3) $$PSF_{total}(\vec{s},\vec{t}) = R_{total}d(\vec{s}-\vec{t}) + PSF_{total}^{stray}(\vec{s},\vec{t})$$

Assuming that scattering is the only source of the stray light, the portion of specular light after the ith mirror is reduced by a factor of $(1\text{-}TIS_i)$. Thus after a series of mirrors i, i=1,2…, the remaining percentage of specular light is reduced to

(3.4) $$R_{total} = \prod_i (1 - TIS_i) \approx 1 - \sum_i TIS_i \ .$$

Note here we have made an approximation to drop terms of the order of TIS^2, which is appropriate when TIS for each mirror is small (cf. Table 2.1). By the same 1^{st} order approximation, the stray part of PSF can be expressed as a sum of stray light contribution from each mirror, i.e.,

(3.5) $$PSF_{total}^{stray}(\vec{s},\vec{t}) = \sum_i PSF_i^{stray}(\vec{s},\vec{t}) \ .$$

This approximation amounts to the following statement in words: a particular stray ray entering a detector can be thought as being scattered **only once** by a mirror precedes the FPA, this particular ray is to follow a specular path **before** and **after** the scattering event at the mirror.

As shown below, this approximation will significantly facilitate a simple algorithm to be implemented so that a detailed and accurate PSF can be calculated numerically.

Substituting Equations (3.3), (3.4), and (3.5) into Equation (3.1), we get

$$(3.6)\qquad M_{\det}(\vec{t}) = \left(1 - \sum_i TIS_i\right) M_{scene}(\vec{t}) + \sum_i \int PSF_i^{stray}(\vec{s},\vec{t}) M_{scene}(\vec{s})\, d^2\vec{s}.$$

Note that we need to impose the normalization condition (Equation 3.2) to the PSF after we obtained the PSF from Equation (3.6).

3.1 Algorithm for determining the end-to-end system level PSFs

To calculate the $PSF^{stray}_i(\mathbf{s},\mathbf{t})$, we need to sum over rays coming from scene at pixel **s**, and end up in detector at pixel **t**. As stated in the last section, we consider those rays scattered only once by the ith mirror, and before and after the scattering event at the ith mirror, each of the rays follows a specular path.

We first fire a bunch of rays from the incident angle corresponding to pixel **s**, trace them specularly until they hit the ith mirror. The area these rays hit on the mirror is $A_{for}(\mathbf{s})$. We then fire a bunch of rays from FPA corresponding to pixel **t**, trace them backward specularly until they hit the ith mirror. The area these rays from FPA hit on the mirror is $A_{aft}(\mathbf{t})$. Because only rays that follow specular paths before and after they hit the ith mirror contribute to PSF^{stray}_i, we only need to sum those rays in the overlapped region $A_i(\mathbf{s},\mathbf{t})$, i.e.,
$A_i(\mathbf{s},\mathbf{t}) = A_{for}(\mathbf{s}) \cap A_{aft}(\mathbf{t})$.

For each point $\mathbf{r}_i$ within the area $A_i(\mathbf{s},\mathbf{t})$, denote the incident direction of a ray specularly hit on it to be $\mathbf{w}_{in}(\mathbf{r}_i,\mathbf{s})$, and the outgoing direction of the ray starting from $\mathbf{r}_i$ and specularly hit the FPA at pixel **y** to be $\mathbf{w}_o(\mathbf{r}_i,\mathbf{t})$, we can obtain the PSF^{stray}_i from the BRDF of the ith mirror by the following integration

$$(3.7)\qquad PSF_i^{stray}(\vec{s},\vec{t}) = \frac{1}{A_i(\vec{s}=0,\vec{t}=0)} \int_{A_i(\vec{s},\vec{t})} BRDF_i\left[\hat{w}_{in}(\vec{r}_i,\vec{s}), \hat{w}_o(\vec{r}_i,\vec{t})\right] \cdot \left[\hat{w}_o(\vec{r}_i,\vec{t}) \cdot \hat{n}_i(\vec{r}_i)\right] d^2\vec{r}_i$$

where $A_i(\mathbf{s}=0,\mathbf{t}=0)$ is the overlap area when **s**=0 and **t**=0. The $1/A_i(\mathbf{s}=0,\mathbf{t}=0)$ factor is to ensure a proper normalization.

The main difference between our algorithmic implementation of Equation (3.7) and those of Monte-Carlo algorithm lies in the details of carrying out the integration. The present method calculates Equation (3.7) by summing over a homogeneous mesh on the ith mirror for a given pair of (**s**,**t**) while-as the MC calculates the integration by stochastic method.

Usually, one would like to work with a PSF with a nice property called shift-invariance so that the Fast Fourier Transform can be used to facilitate the calculation. A shift-invariant PSF is a function only depends on the difference of it two arguments, which is **s-t** in our notation. Unfortunately, the PSF obtained so far does not have this property due to the so-called vignetting effect. To make this point more clear, lets first define the following vignetting function for the ith mirror

$$(3.8)\qquad V_i(\vec{s},\vec{t}) = \frac{A_i(\vec{s},\vec{t})}{A_i(0,0)},$$

where $A_i(\mathbf{s},\mathbf{t})$ is the same as in Equation (3.7).

For **s** and **t** within the designed FOV ($15^{o}\times1.256^{o}$ in the case of the ALI), the vignetting function is by design to be one, i.e., no field darkening within the FOV. As **s** increases beyond the FOV, the vignetting function starts to decrease from one because some of the rays are blocked by the baffles so that $A_i(\mathbf{s},\mathbf{t})$ will become smaller than $A_i(\mathbf{s}=0,\mathbf{t}=0)$. Since we are only interested in cases when **t** is within the FOV, the vignetting function can be approximated as a function of **s** only.

Having defined the vignetting function, we can rewrite the PSF as

(3.9) $$PSF_i^{stray}(\vec{s},\vec{t}) = V_i(\vec{s})psf_i^{0}(\vec{s},\vec{t}).$$

This would be nothing more than introducing a new function psf^0 were it not for the fact that by separating out the shift-invariance-spoiler, the vignetting function $S(\mathbf{s})$, psf^0 is found to be a good shift-invariant function and this has been verified in our numerical calculations. It is clear that we can obtain psf^0 from Equations (3.7), (3.8) and (3.9).

4. Results of the ALI System Level Point Spread Function

As we have discussed in the previous sections, the stray part of PSF can be written as

(4.1) $$PSF_{total}^{stray}(\vec{s},\vec{t}) = \sum_i V_i(\vec{s})\, psf_i^0(\vec{s}-\vec{t}),$$

where i is the mirror index, $V_i(\mathbf{s})$ is the vignetting function, and $psf_i^0(\mathbf{s}-\mathbf{t})$ is a shift-invariant function, i.e., a function of $(\mathbf{s}-\mathbf{t})$ only.

In order to present our results more clearly, we define the the following 8 azimuth directions as shown in Figure 4.1. The x, and y direction are the instrument directions as shown in Figure 1.1.

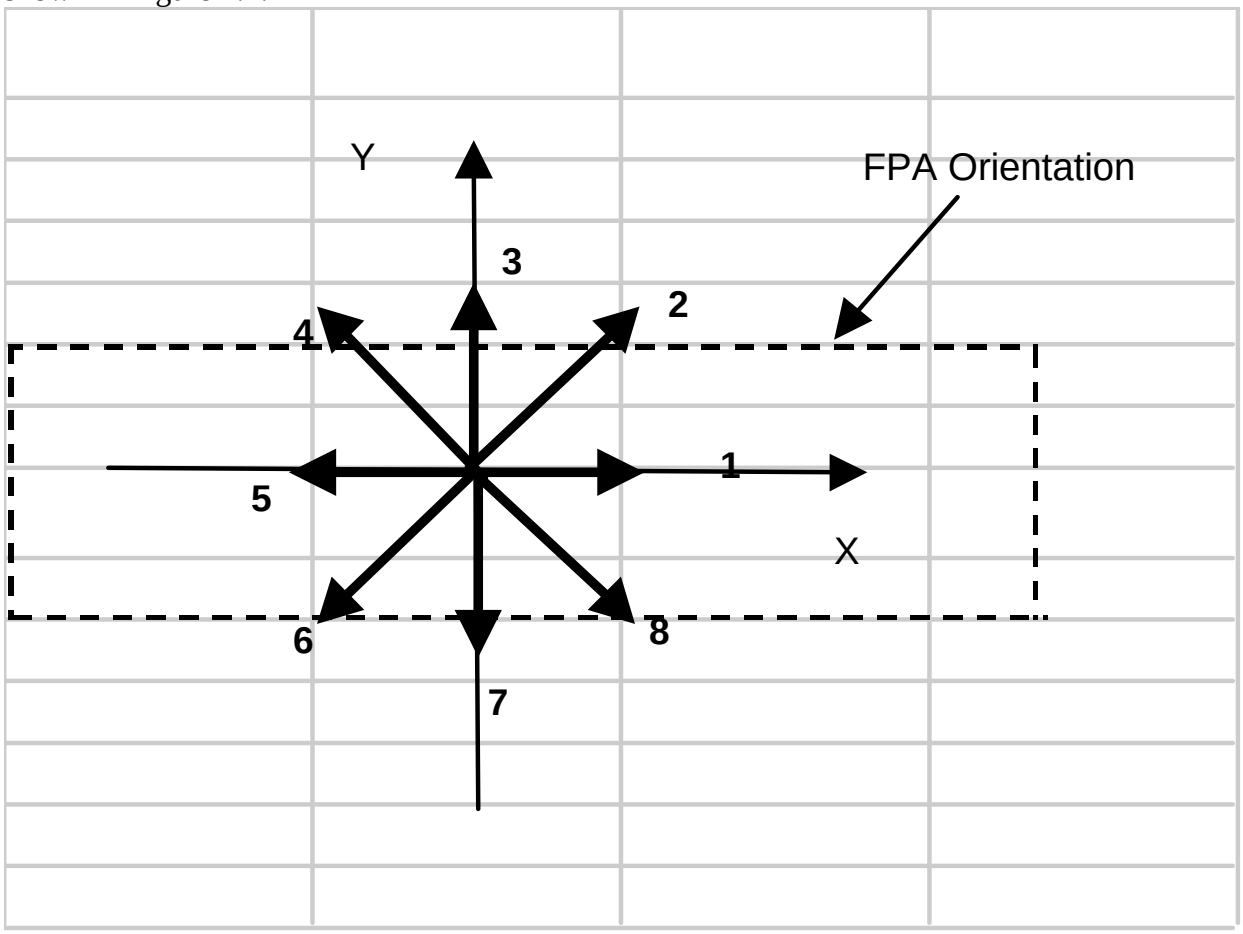

Figure 4.1 Illustration of the 8 directions along which the PSFs are plotted. Coordinate system is the same as noted in Figure 1.1.

In Figures 4.2-4.5, we show the function $psf_i^0(\mathbf{s})$ along the 8 directions defined in Figure 4.1, for M1, M2, M3, and F1 mirrors respectively. In these figures $\theta=|\mathbf{s}|$. Also shown in these figures are fitting functions of the following form

(4.2) $$psf_i^0(\vec{s}) = \frac{a_i \cos(q)}{b_i + |\sin(q)|^{h_i}}, \quad q = |\vec{s}|,$$

where the parameters are tabulated in Table 4.1 for the four mirrors.

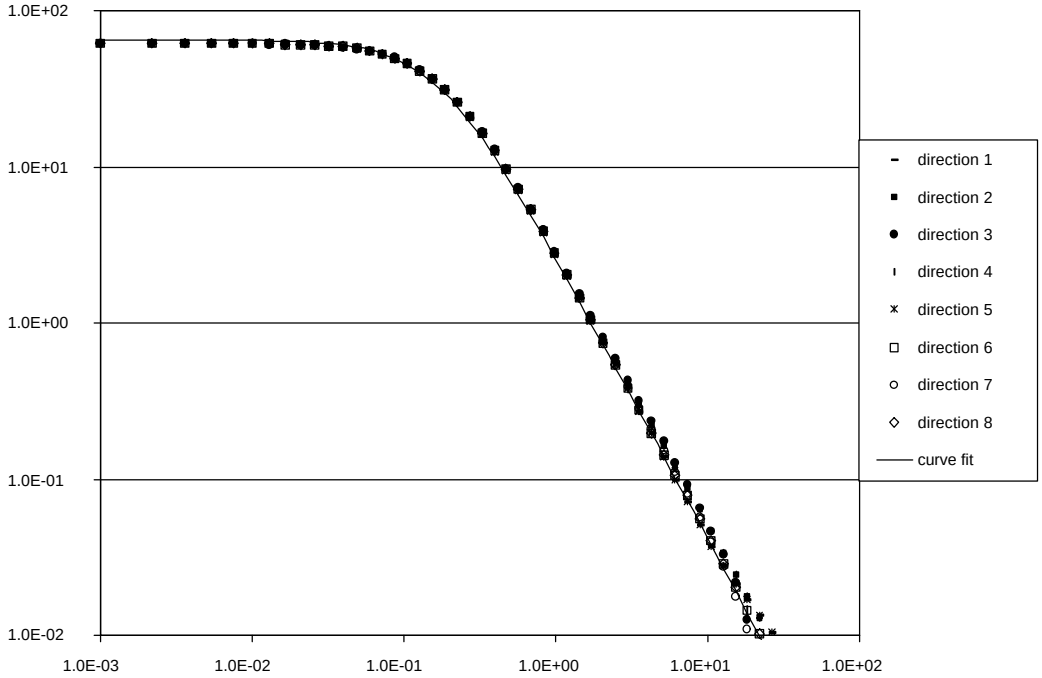

Figure 4.2 $psf_i^0(\mathbf{s})$ for the M1 mirror along 8 directions defined in Figure 4.1

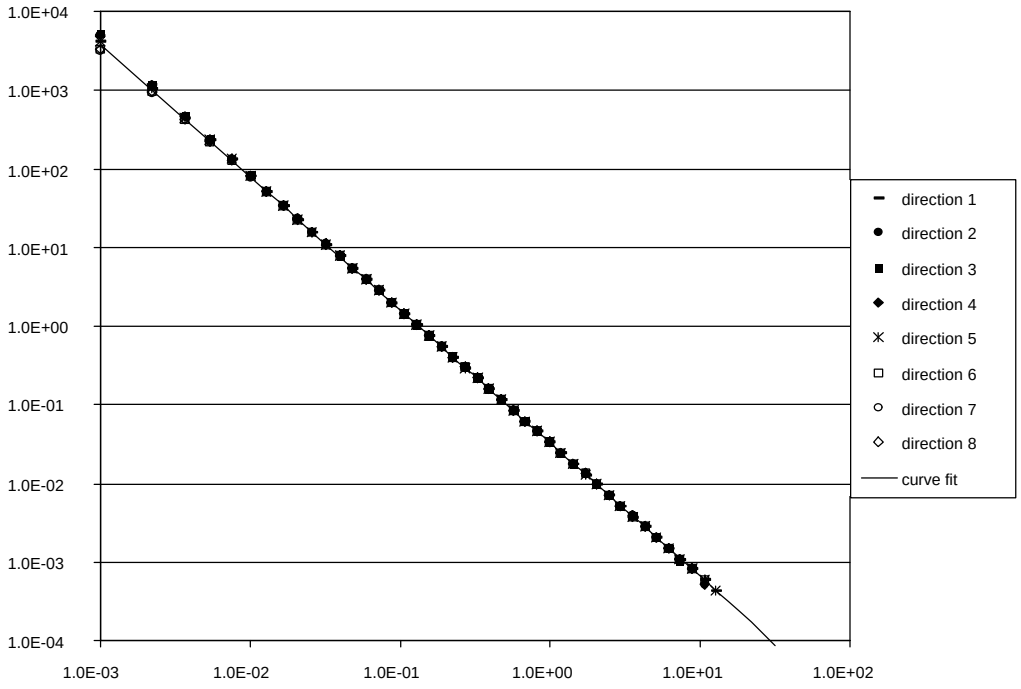

Figure 4.3 $psf_i^0(\mathbf{s})$ for the M2 mirror along 8 directions defined in Figure 4.1

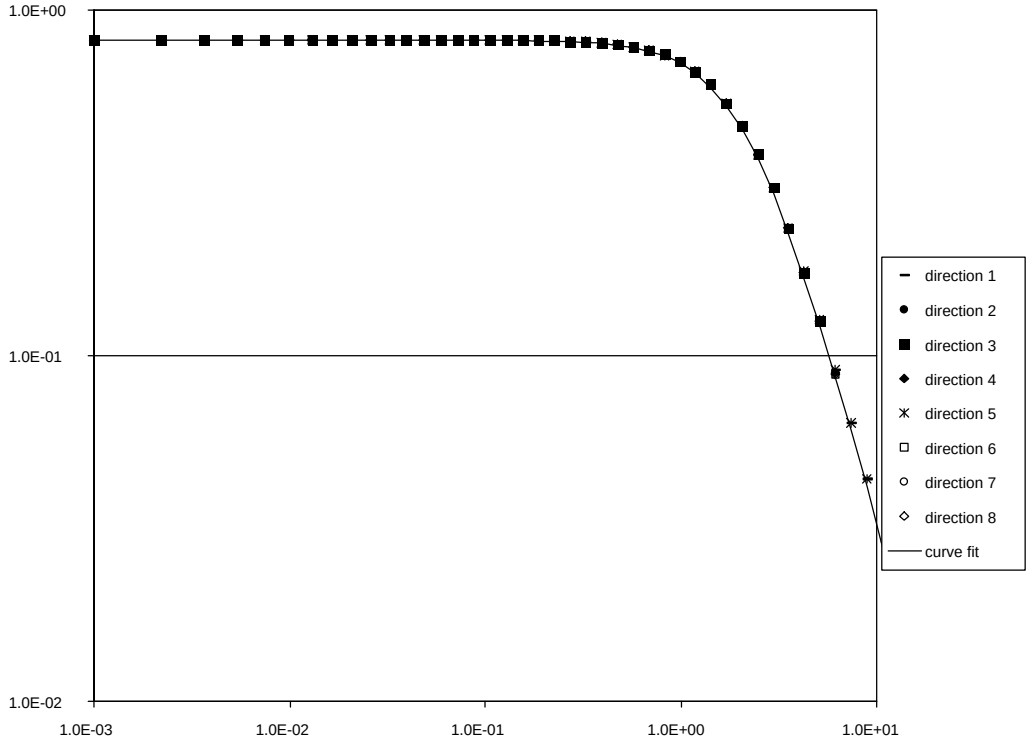

Figure 4.4 $psf_i^0(\mathbf{s})$ for the M3 mirror along 8 directions defined in Figure 4.1

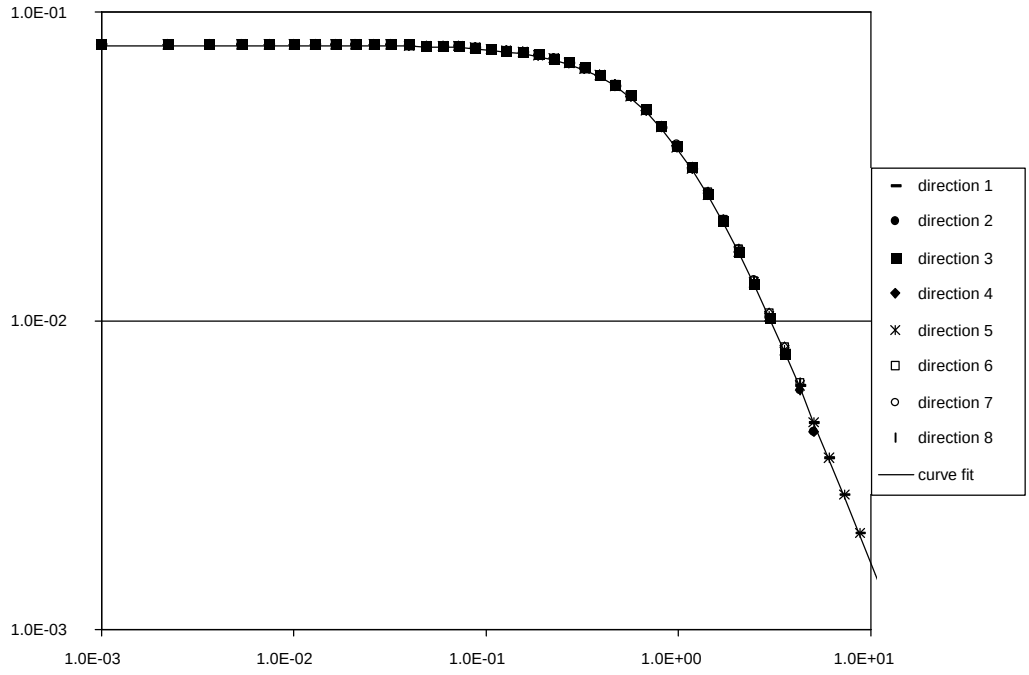

Figure 4.5 $psf_i^0(\mathbf{s})$ for the F1 mirror along 8 directions defined in Figure 4.1

Table 4.1 Fitting parameters for $psf_{\alpha}^{0}(\mathbf{s})$ (c.f. Equation 4.2)

λ=633 nm	M1	M2	M3	F1
a	1.81e-3	3.48e-5	8.1e-4	1.06e-4
b	2.81e-5	1.e-10	9.1e-4	1.36e-3
h	1.80	1.69	2.14	1.59

It is expected that without vignetting, point spread functions follow closely those of the BRDFs. We should **not**, however, expect the parameters to be the same as those in the BRDFs, because each mirror's norm is not along the nadir direction and for mirrors other than M1, incident ray angles do not coincide with θ.

The total $PSF_{total}^{stray}(\mathbf{s},\mathbf{t}=0)$ is shown in Figure 4.6, as we can see, after the vignetting effect is included, the $PSF_{total}^{stray}(\mathbf{s},\mathbf{t}=0)$ shows the expected asymmetry. We note that this asymmetry is mainly due to the vignetting effect of the fore-baffle. Increasing the distance between the fore-baffle and the M1 mirror will more efficiently suppress the large off-axis angle scattering contribution. Doing so will, however, also decrease the designed FOV.

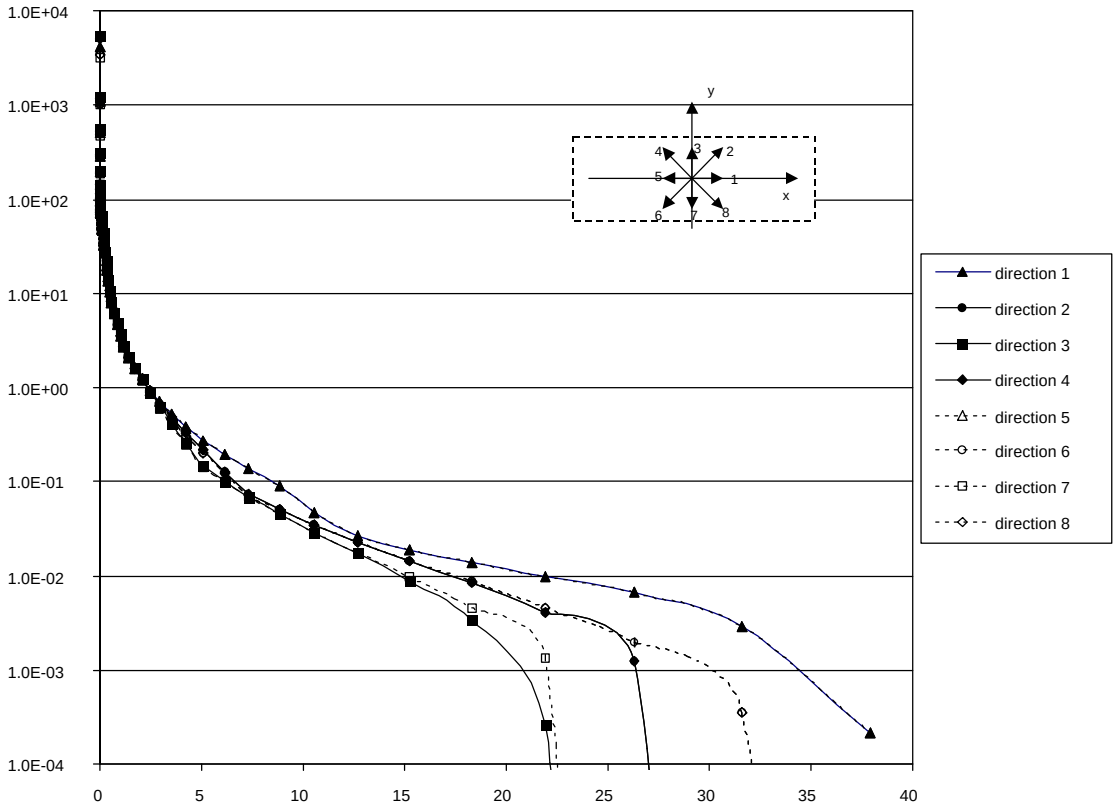

Figure 4.6 $PSF^{stray}(\mathbf{s},\mathbf{t}=0)$ for the ALI along the 8 directions defined in Figure 4.1.

5. Convolving the System Level PSF with Selected Scenes to Determine the ALI Scattered Light Performance

5.1 Landsat 7 system specification revision K compliance

The Landsat 7 System Specification Revision K (July 1997) states:

" **The response of an ETM+ detector to off-axis levels of stray radiation is defined as the change in detected signal that results when a radiance scene of specific level and annular solid angle FOV surrounds, and is centered on, an extended target FOV radiance scene that produced the baseline detected signal and on which the detector channel IFOV is centered.**
…
The off-axis radiance of all channels for the ETM+ panchromatic and Spectral Bands 1, 2, 3, 4, 5 and 7 shall be less than 2% of the nominal full-scale signal level (Reference 3.7.8.1.7) for the extended target FOV scene size and radiance levels and the stray radiance scene annular size and radiance levels shown in Table" 5.1.

This specification scene is illustrated in Figure 5.1. Table 5.1 defines the extended FOV target and the Stray Radiation Scene (SRS) for band 3 and the pan band. For the annular radii in the table, we have also shown the corresponding number of pixels with respect to the respective pixel size, e.g., for band 3 it is 40μr per pixel, and for the pan band it is 14μr per pixel.

Table 5.1 Landsat 7 System Specification Revision K Scene

Extended FOV Target (Region I)				Stray Radiation Scene (Region III)		
BAND	FOV radius	Scene Radiance mW/[cm^2 -sr-µm]	Low Gain Saturation Radiance mW/[cm^2-sr-µm]	Inner Annular Radius	Outer annular radius	Radiance mW/[cm^2 -sr-µm]
Pan.	128 µr (~9 pixels)	2.285	22.5	384 µr (~27 pixels)	0.436 r (~3114 pixels)	44.05
3	128 µr (~3 pixels)	2.167	23.5	384 µr (~10 pixels)	0.436 r (~10900 pixels)	48.31

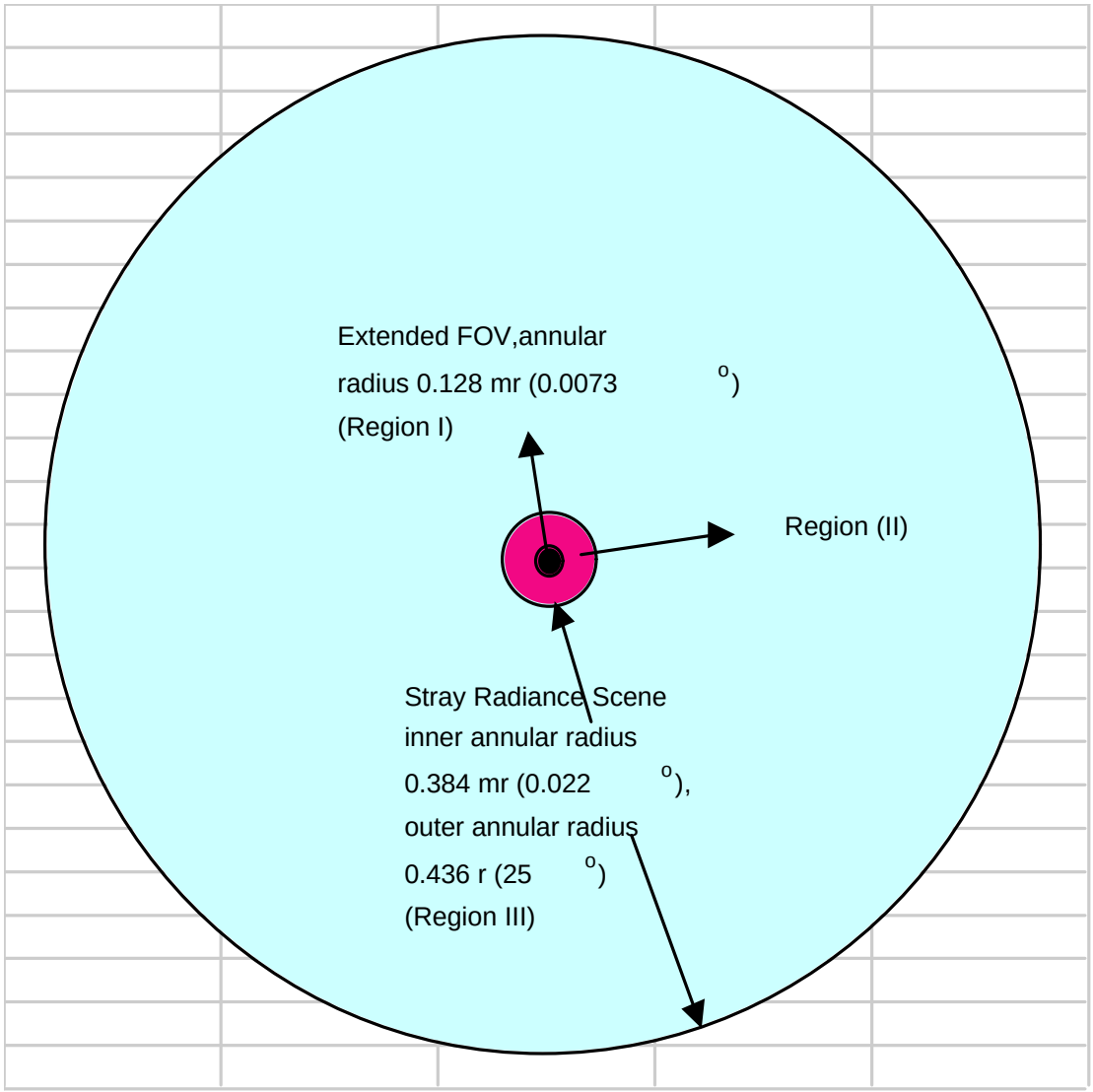

Figure 5.1 Illustration of the Landsat 7 system specification revision K

The detected baseline signal at the center of the target FOV produced by the Stray Radiation Scene is calculated by

$$(5.1) \qquad M_{base}(0) = M_{SRS} \int_{q_1}^{q_2} dq \int_{0}^{2p} PSF_{total}^{stray}(\vec{x}, 0) dj, \quad q_1 = 384mr, \quad q_2 = 0.436r.$$

Using the previously obtained PSF, the calculated M_{base} for band 3 and the panchromatic band is shown in Table 5.2. The percentages of this baseline signal with respect to the target radiance and the low gain saturation radiance are also shown in Table 5.2.

Apparently, the off-axis contribution well exceeds the spec if we take the full scale nominal radiance to be that of the target radiance. We note, however, if the mirrors, especially M1 and M3, are of as good a quality as the mirror M2, the compliance with the spec will be greatly improved. Table 5.3 shows the improved results if all the ALI mirrors are as good as the M2 mirror or as good as the MODIS FM2 scan mirror.

Table 5.2 Baseline radiance at the center of target FOV from the SRS

Band	Baseline radiance from SRS mW/[cm^2-sr-μm]					% of target radiance	% of low gain saturation radiance
	M1	M2	M3	F1	Total		
Pan.	1.03	0.01	0.21	0.01	1.26	55%	5.4%
3	1.35	0.01	0.37	0.01	1.74	80%	7.7%

Table 5.3 Results for baseline radiance as in Table 5.2 with improved mirrors

Band	% of target radiance if all mirrors are as good as M2	% of target radiance if all mirrors are as good as the MODIS FM2 scan mirror
Pan.	3.4%	<1%
3	4.0%	<1%

We have also studied how the baseline level will decrease as we increase the inner annular radius of the Stray Radiation Scene (SRS) while keeping its outer radius fixed. The result for the band 3 is shown in Figure 5.2.

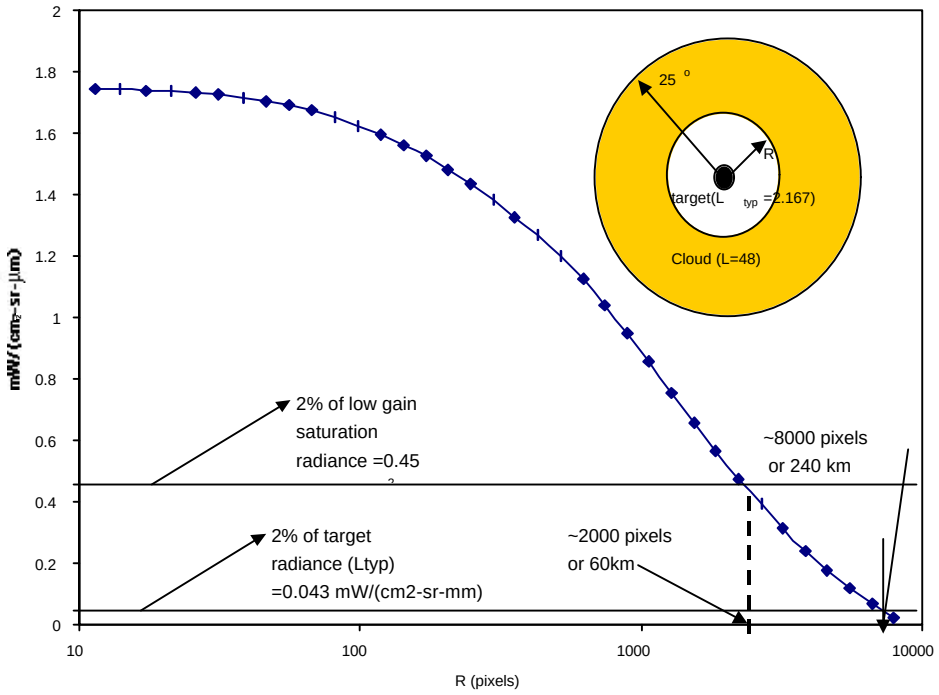

Figure 5.2 For band 3 baseline radiance from SRS vs. the inner radius (in pixels).

As is clear from Figure 5.2, in order for the off-axis contribution from the SRS to be less than 2% of the target radiance, the SRC has to be pushed as far out as several thousands of pixels away from the target.

5.2 Cloud edge transient response analysis

An edge scene is a sharp edge dividing a bright (unit radiance) and a dark (zero radiance) region. We have studied the following four edge semi-infinite cloud edge scenes (in unit of mW/cm^2-sr-μm):

$$(5.2.a)\quad M(x,y)=\begin{cases}48.31 & x<0\\ 2.167 & x>0\end{cases}$$

$$(5.2.b)\quad M(x,y)=\begin{cases}2.167 & x<0\\ 48.31 & x>0\end{cases}$$

$$(5.2.c)\quad M(x,y)=\begin{cases}48.31 & y<0\\ 2.167 & y>0\end{cases}$$

$$(5.2.d)\quad M(x,y)=\begin{cases}2.167 & y<0\\ 48.31 & y>0\end{cases}.$$

For each of these scenes, the following convolutions are performed using our calculated PSF

$$(5.3.a)\quad M_{\det}(x,y=0)=48.31\int dy'\int_0^{\infty}dx'\,PSF_{total}(x',y';x,y=0)+2.167\int dy'\int_0^{\infty}dx'PSF_{total}(x',y';x,y=0)$$

(5.3.*b*) $$M_{\det}(x, y=0) = 2.167\int dy' \int_{0}^{0} dx' PSF_{total}(x', y'; x, y=0) + 48.31\int dy' \int_{0} dx' PSF_{total}(x', y'; x, y=0)$$

(5.3.*c*) $$M_{\det}(x=0, y) = 48.31\int dx' \int_{0}^{0} dy' \; PSF(x', y'; x=0, y) + 2.167\int dx' \int_{0} dy' PSF_{total}(x', y'; x=0, y)$$

(5.3.*d*) $$M_{\det}(x=0, y) = 2.167\int dx' \int_{0}^{0} dy' \; PSF(x', y'; x=0, y) + 48.31\int dx' \int_{0} dy' PSF_{total}(x', y'; x=0, y)$$

The results for the four cases, (a), (b), (c), and (d), where y axis is $\Delta L/L_{typ}$, are shown in Figures 5.3-5.6.

We note the stray-radiance at same distance from the edges is smaller for the y-edges than for the x-edges. This is because the FOV is much narrower along the y-direction so that the vignetting effect due to the fore-baffle is much stronger for the y-edges.

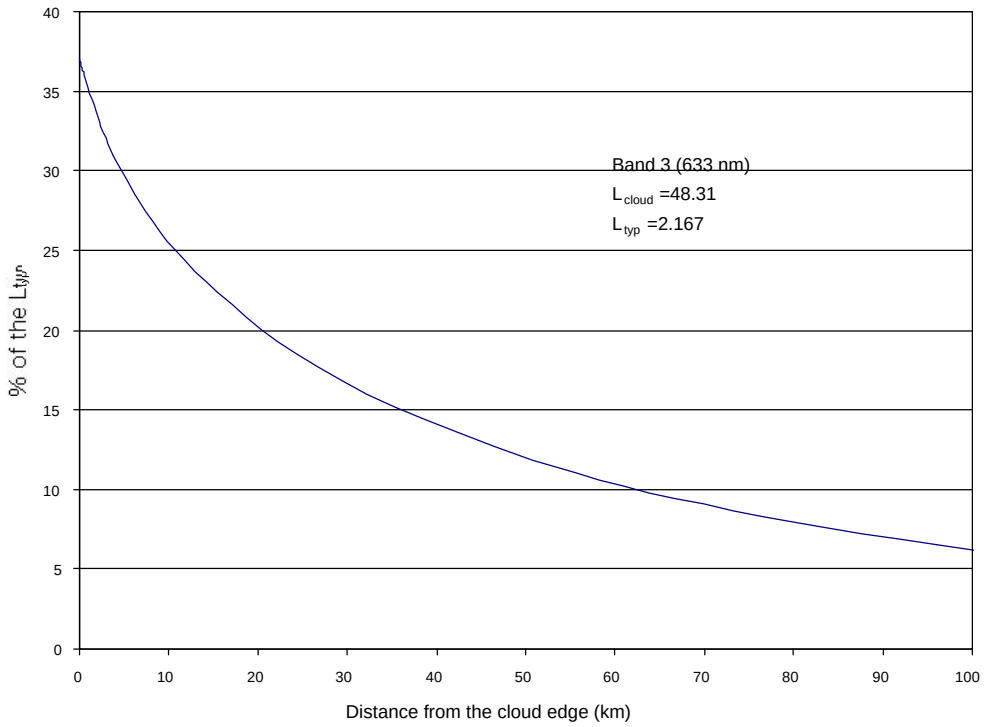

Figure 5.3 ΔL/L of the convolved edge scene as defined in Equation (5.3.a).

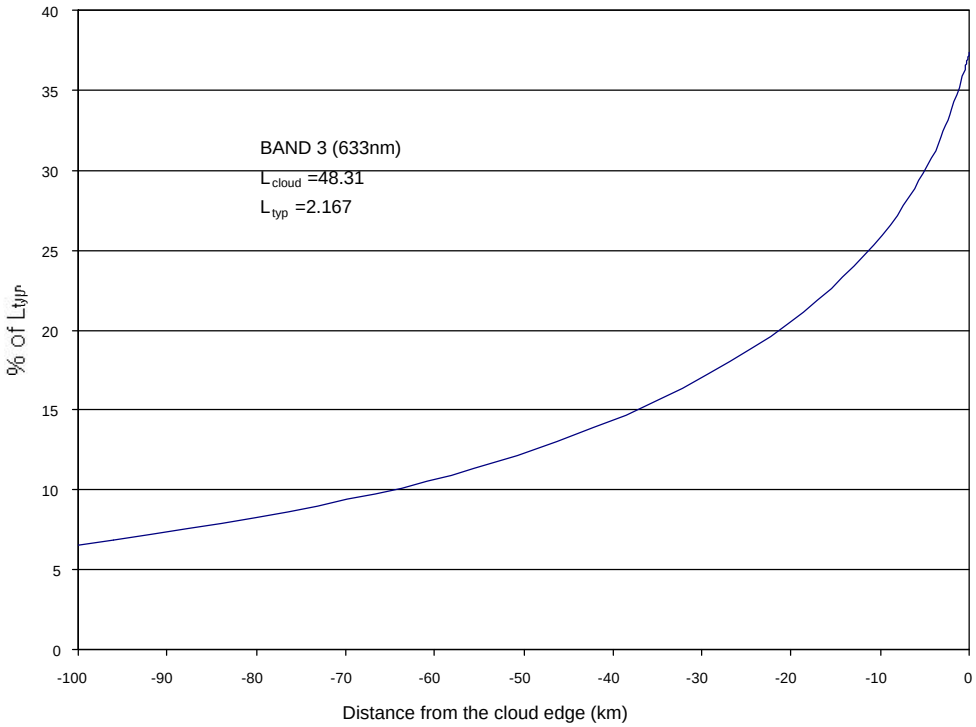

Figure 5.4 ΔL/L of the convolved edge scene as defined in Equation (5.3.b).

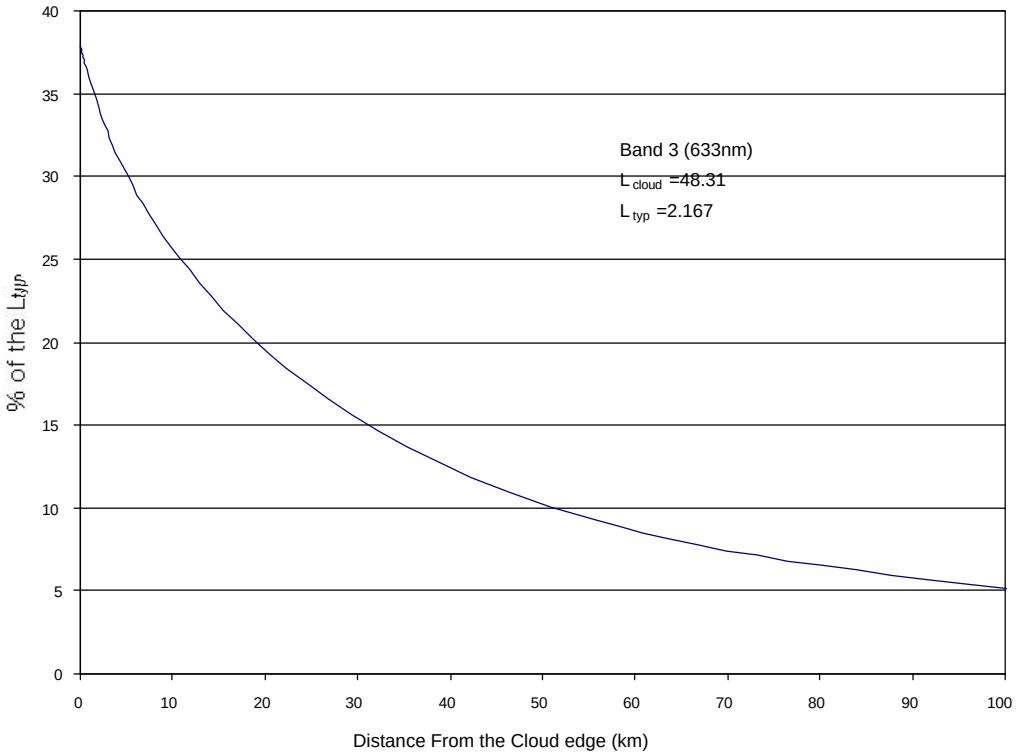

Figure 5.5 ΔL/L of the convolved edge scene as defined in Equation (5.3.c).

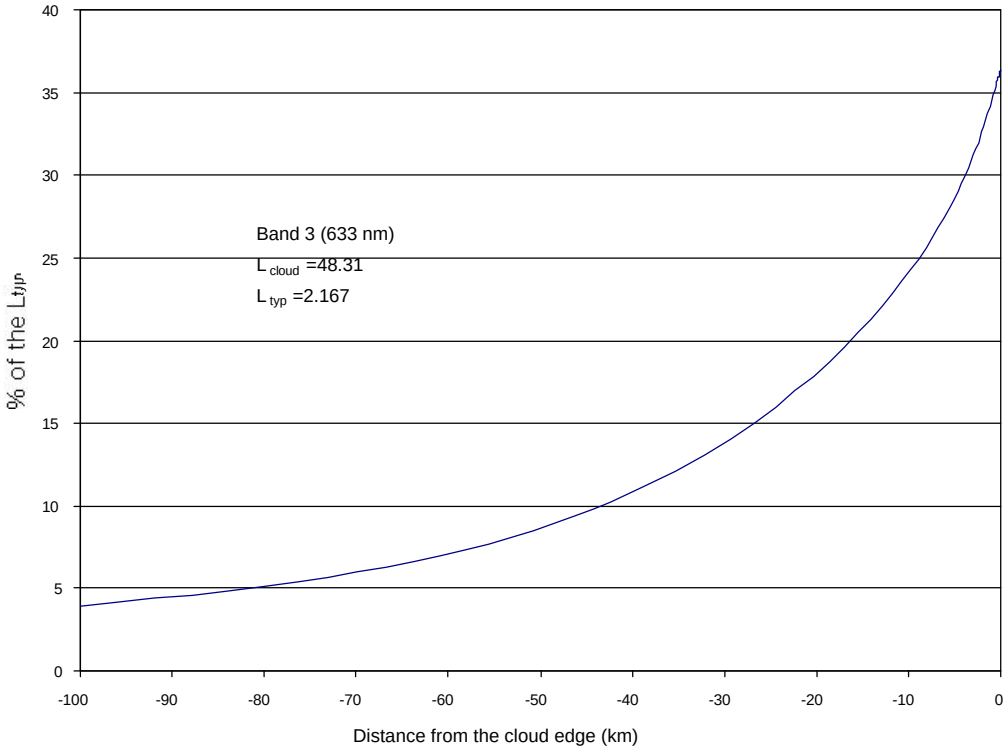

Figure 5.6 ΔL/L of the convolved edge scene as defined in Equation (5.3.d).

In Figures 5.7-5.10, we plotted the same cloud edge transient responses assuming all four mirrors are as good as the M2 mirror, i.e., they all have the same TIS. These plots demonstrate that if all the mirrors can be made as good as M2 or even better, the wide angle FOV of the ALI design may be acceptable.

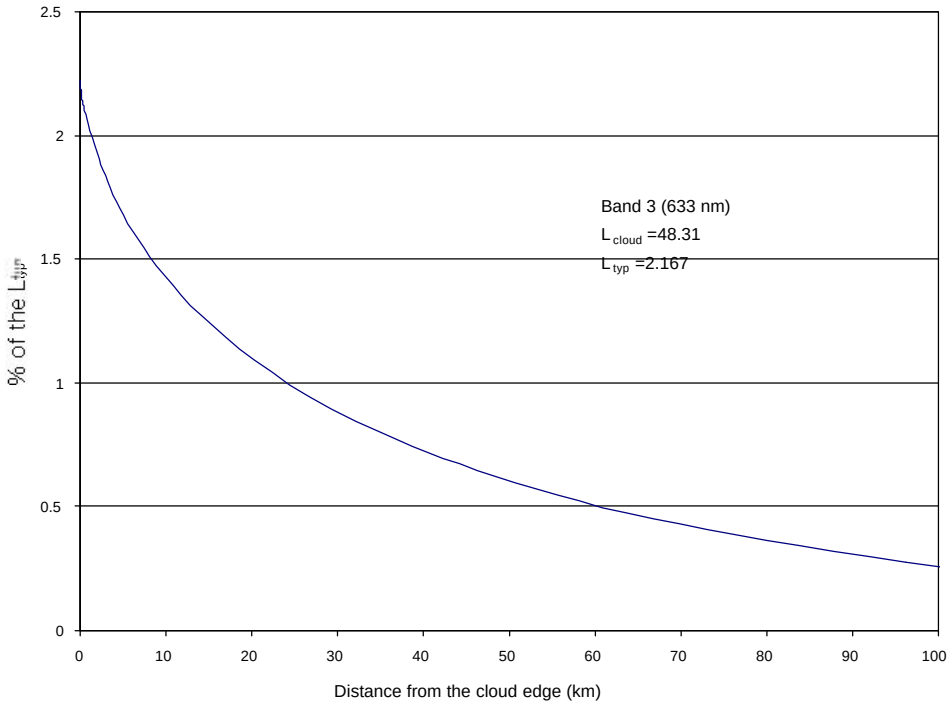

Figure 5.7 ΔL/L of the convolved edge scene as defined in Equ. (5.3a) with all mirrors as good as M2.

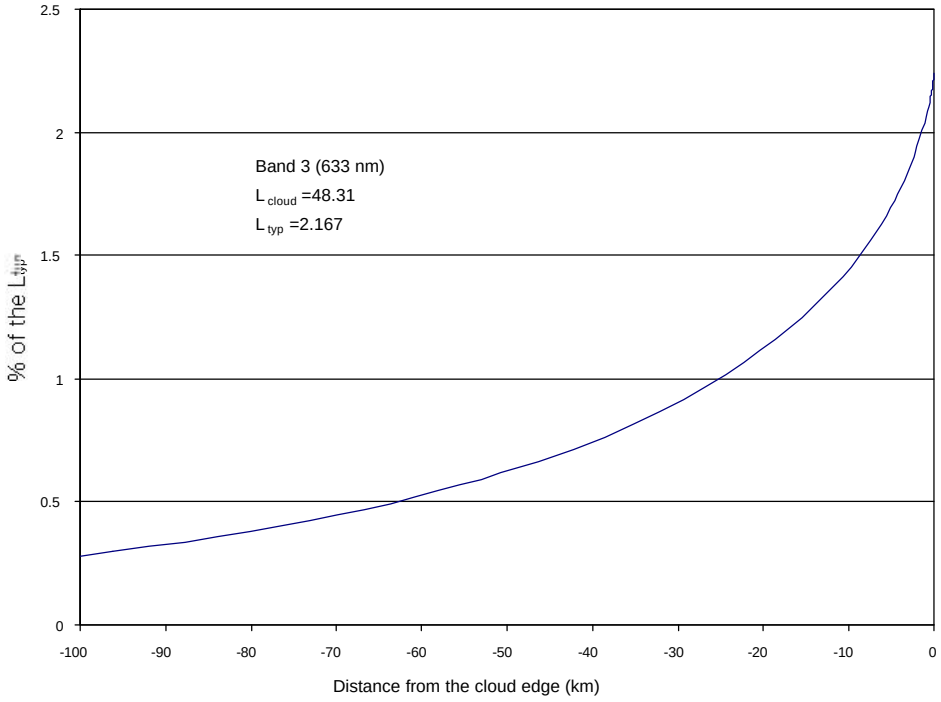

Figure 5.8 ΔL/L of the convolved edge scene as defined in Equ.(5.3b) with all mirrors as good as M2.

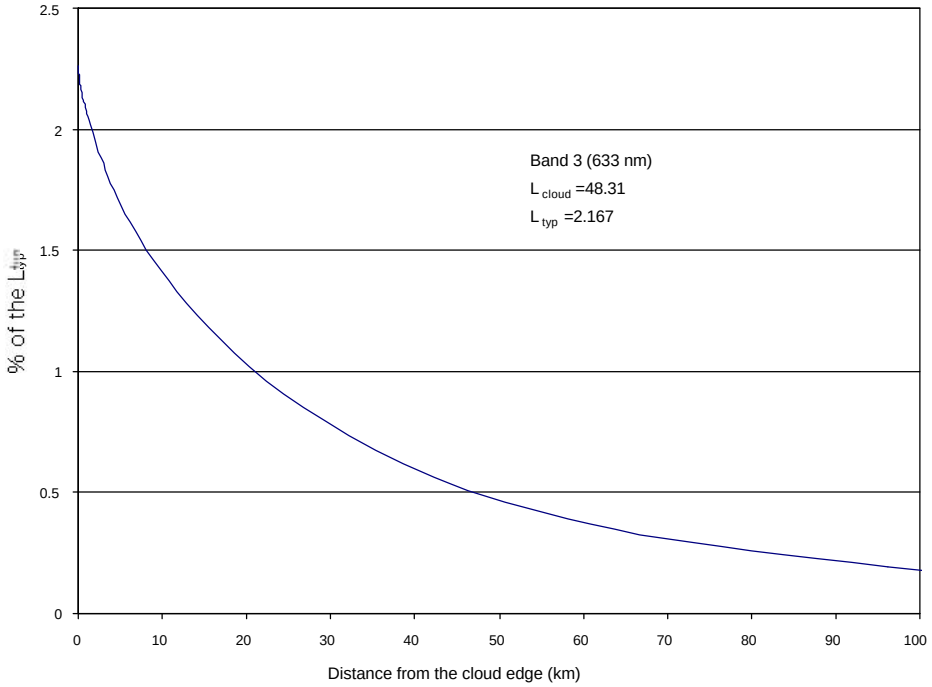

Figure 5.9 ΔL/L of the convolved edge scene as defined in Equ. (5.3c) with all mirrors as good as M2.

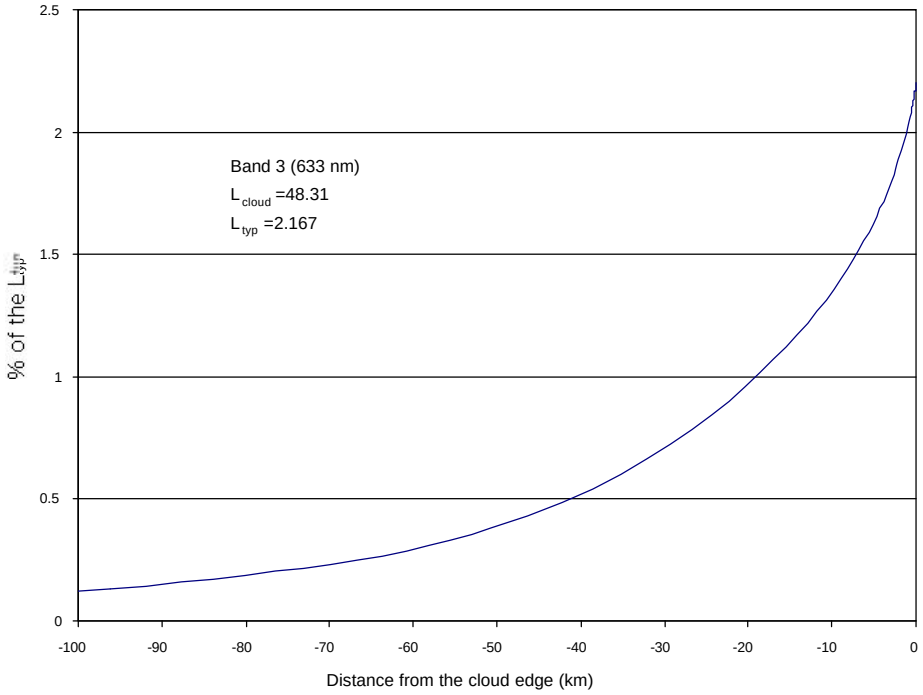

Figure 5.10 ΔL/L of the convolved scene as defined in Equ. (5.3d) with all mirrors as good as M2.

5.3 Convolution of realistic scenes

We have convolved two more realistic scenes for band 3 and the panchromatic band. Here we will present a very brief analysis of the convolved scenes. Figure 5.11 shows a one-dimensional slice of one of the scenes for band 3. Figure 5.12 shows $\Delta L/L_{original}$ values for the same slice where $\Delta L=L_{convolved}-L_{original}$. We can see that for low contrast scenes, the performance of the ALI is much better than for cloud edge scene. As expected, the relative errors are off-phase with respect to the scene.

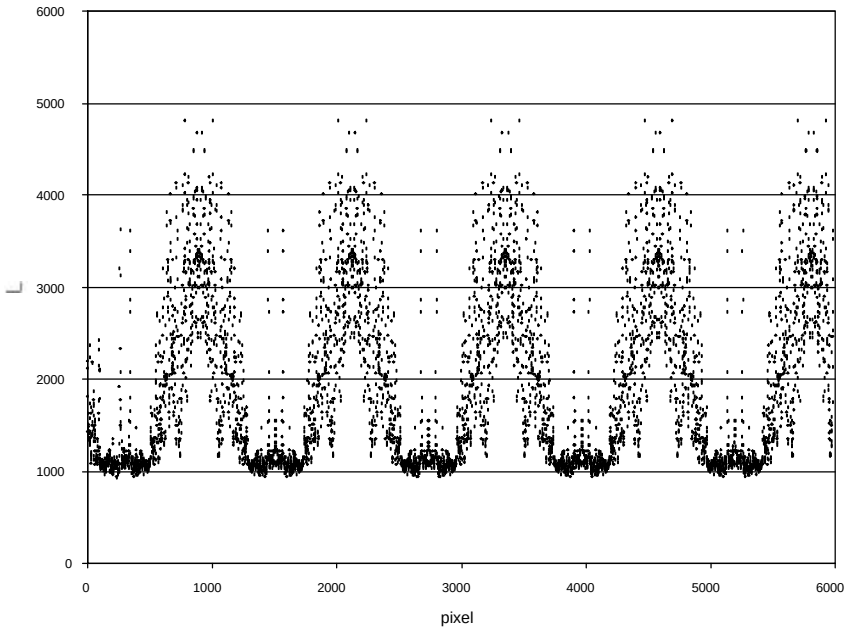

Figure 5.11 A one-dimensional slice of a more realistic scene.

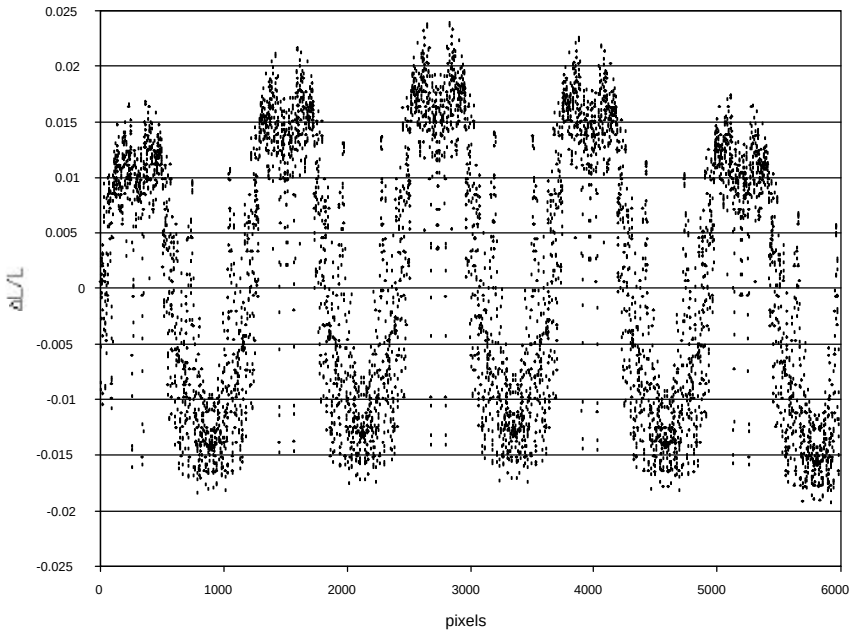

6. Summary and Conclusions

We have obtained the system-level point spread function due to scattering for the ALI telescope. The system-level PSF model we have developed for the Panchromatic Band and Band 3 has been applied to various synthetic and Earth data scenes. Based on our analysis, we conclude the following:

1). For the current mirrors, the wide FOV of the ALI is going to cause significant radiance bias errors in the presence for high contrast scenes, such as a cloud edge, even if the bright cloud is tens of kilometers away. This is mainly due to the fact that a wide FOV design allows the scattered light from a far-away bright source to be registered at the detector without being significantly vignetted. Examples we studied to demonstrate this include the Landsat 7 specification scene and semi-infinite cloud edge scene. For the Landsat 7 spec scene, the scattered light radiance levels at the center of the specified scene were found to be 55% and 80% of the target radiance levels, for the Pan Band and Band 3, respectively. In terms of the low gain saturation radiance levels, the scatter levels were found to be 5.4% and 7.7%, for the Pan Band and Band 3, respectively. When the PSF was applied to more physically realizable scenes, such as a semi-infinite straight cloud edge with a contrast ratio given by L_{cloud}/L_{typ} of 22.3, it was found that the scatter levels will be greater than 10% of the L_{typ} values for scene pixels 50 to 60 km from the cloud edge. These relatively high levels of scatter, extending over long distances from the specular point, suggest that efforts to restore images by applying FFT inversion techniques will require very detailed and accurate knowledge of the actual PSFs over a large area, which is not likely, considering the very challenging measurement requirement.

2). We note, however, there is still much room for improvement in terms of mirror quality. We found that if all the mirrors are as good as the M2 mirror of the ALI, the performance of the telescope can be greatly enhanced such that the relative errors for the spectral radiance can almost meet the 2% requirement even for the semi-infinite cloud edge scene. In light of the fact that these mirrors are made of the same SiC material, we believe that by improving the fabrication technique in making these mirrors, the ALI will be able to meet even the most stringent specification. These results suggest that a wide FOV push-broom sensor could be effective, provided the mirror surfaces are maintained at very low cleanliness levels (< CL300).

Acknowledgements:

We thank the MIT Lincoln Laboratory for providing the essential instrument description materials, and a copy of the Lambda Research Corporation excellent ALI scattered light analysis report. Further, we want to thank Dr. E. Waluschka (from GSFC Code 700) for helpful discussions regarding the code V sequence file for the ALI telescope, and Schmidt Measurement Systems for the BRDF data for the four mirrors. We also want to thank Nick Speciale and Dr. Steve Ungar for constant support and useful discussions throughout the course of this study. This work was supported by the New Millenium Program Earth Orbiter-1 Project.